Additive Manufacturing 54 (2022) 102779

Contents lists available at ScienceDirect

Additive Manufacturing

journal homepage: www.elsevier.com/locate/addma

Research Paper

Quantitative study on the dynamics of melt pool and keyhole and their controlling factors in metal laser melting

Ming Wei, Wen Jun Ding, Guglielmo Vastola *, Yong-Wei Zhang *

*A*STAR Institute of High Performance Computing, 1 Fusionopolis Way, #16-16 Connexis, 138632, Singapore*

ARTICLE INFO

Keywords:
Melt pool dynamics
Keyhole dynamics
Keyhole oscillation
Bubble formation

ABSTRACT

Recent direct visualization of keyhole morphology evolution by ultrahigh-speed synchrotron X-ray imaging provides fascinating insights and basis for further understanding and investigation of the melt pool (MP) behavior during laser melting. By combining the ray-tracing method, the phase field method and the lattice Boltzmann method, we simulate the laser melting process of Ti-6Al-4V plates quantitatively and predict five distinct regimes observed experimentally, and uncover the underlying dynamics and controlling factors for each regime. Remarkably, we also reveal four types of distinct oscillations of the MP and their underlying mechanisms. The 3D irregular oscillation of keyhole tip is identified to be responsible for bubble spill-over. These revealed dynamics and their underlying controlling factors provide a solid physical foundation for controlling laser-based 3D printing processes.

1. Introduction

Laser materials processing is at the forefront of processing technology and is currently widely adopted in many industrial processes, including laser welding, surface engineering, additive manufacturing, and laser drilling. The range of materials in these applications covers metals, plastics, semiconductors and ceramics, on a scale from submicron to several meters [1–3]. In laser processing, the material first melts from the surface and subsequently forms a melt pool (MP). In this process, electromagnetic energy is rapidly absorbed by the material, resulting in high heating and cooling rates, as well as large thermal gradients. Such strong energy transfer induces additional phenomena such as spattering, denudation, keyhole formation, and cracking [4–6].

At a high energy density, a keyhole is formed by the reaction force (recoil pressure) resulting from flash evaporation of the molten metal [7–9]. Although the formation of the keyhole promotes laser permeability and increases laser energy absorption efficiency, its instability may lead to pores, spattering, thermal ablation and other problems [10–12]. The formation of pores, in turn, degrades the mechanical properties of parts produced by laser welding and laser additive manufacturing. Additionally, spattering of powders and melt pool droplets influence the stability of melting pool and surface roughness, while thermal ablation can change the alloy composition, phase constitution and microstructure. Although the mechanism of keyhole formation and oscillation has been investigated in several studies [13–17], an in-depth understanding of the mechanism which enables or suppresses the formation of keyhole remains elusive. Clearly, such understanding is of paramount importance to the ability of controlling porosity, and thus part quality in laser processing.

Along with the development of synchrotron-based X-ray tomography technology, recent in-situ observation of keyhole behavior has provided quantitative data to study keyhole formation, morphological evolution, and instability [18–22] with spatial and temporal resolutions of micro meter and micro second, respectively. In particular, Cunningham et al. [16] recently reported high-resolution in-situ observation of MP and keyhole morphological evolutions in Ti-6Al-4V under different processing conditions. Under typical laser powers, their work clearly identified five regimes for the MP formation and evolution: (i) melting, (ii) vapor depression formation and growth, (iii) vapor depression instability, (iv) keyhole formation and growth, and (v) complex shape change of keyhole. These rich experimental results provide a fascinating basis for further exploring their underlying dynamics and controlling factors. In fact, a new evaporation model has already been proposed based on these in-situ experimental results [23]. We note that these five regimes were proposed based on the evolution of MP profile in experiment, however, the underlying rays reflection, temperature distribution, fluid dynamics and driving forces and their controlling factors have not been studied in-depth quantitatively. Clearly, quantitative

* Corresponding authors.
E-mail addresses: vastolag@ihpc.s-star.edu.sg (G. Vastola), zhangyw@ihpc.a-star.edu.sg (Y.-W. Zhang).

https://doi.org/10.1016/j.addma.2022.102779
Received 16 October 2021; Received in revised form 9 February 2022; Accepted 20 March 2022
Available online 23 March 2022

understanding their dynamics and controlling factors are of vital importance for controlling the dynamics and pore formation.

Computational modelling is a powerful tool to study the processes of laser processing. Discrete element method (DEM) has been applied to simulate the power bed packing process [24,25]. Computational fluid dynamics (CFD) methods, for example, volume of fluid (VOF), lattice-Boltzmann method (LBM), and finite volume method (FVM), have been widely applied in the study of melt pool dynamics [26–28]. Phase field (PF) method and the cellular automaton (CA) method have been used to simulate the phase transition and the microstructure evolution [29–32]. Finite element method (FEM) has been applied to investigate the residual stress and thermal stress in laser processing [33,34]. At the same time, integration of multi-scale, multi-physics models becomes critical since the laser processing involves multi-physics phenomena. For example, Chen et al. [35] simulated the spattering and denudation in laser powder bed fusion (LPBF) with DEM and FVM. Liu et al. [36] studied the rapid solidification process of Ti64 alloy with PF and LBM. Lian et al. simulated the microstructure evolution in additive manufacturing (AM) with CA and FVM.

Here, we perform high-fidelity physics-based modeling on the 3D melting of Ti-6Al-4V under stationary laser condition by fully coupling laser ray tracing method, PF and LBM to account for laser energy absorption and reflection, heat transfer, phase transformation and fluid flow. The PF method, using diffuse interface, avoids the numerical challenges related to tracking the interface, and can describe the 3D structure more accurately than sharp-interface models. LBM was chosen because it can be easily parallelized, accelerating large-size three-dimensional simulations. Laser ray tracing method is attractive because it considers the absorption of reflected rays and calculates the actual absorbed energy and its spatial distribution. The modelling results accurately reproduce the five distinct regimes observed in the experiments under typical laser powers, thus validating our physics-based modelling procedure. Beyond, we further reveal the underlying dynamics and controlling factors in each regime during the laser melting and analyze the mechanisms of four type keyhole oscillations. Quantitative dynamic data of melt pool and keyhole for parameter window of production could be predicted accurately from our simulations. These revealed dynamics and their underlying controlling factors provide significantly new insights and powerful guidelines for controlling the laser-based 3D printing processes.

2. Theoretical models and numerical methods

Here, we developed a physics-based modelling procedure aiming at tracking the morphological evolutions of the MP and keyhole during the melting of a bare Ti-6Al-4V plate under a stationary laser and reveal their underlying dynamics and controlling factors. A phase-field model, in which vapor was treated as a conserved phase [29,37], was adopted to model the phase transformation. To incorporate the effects of recoil pressure [38], Marangoni force [39] and evaporation latent heat [40], an improved LBM model based on Ref. [27,41,42] was developed and implemented to account for the MP fluid dynamics. Thermal governing equations were solved by considering thermal diffusion, radiation, surface convection, phase transition latent heat, and laser energy absorption. The phase field model was coupled on-the-fly with a ray tracing model whereby the incidence and multiple reflections of each laser ray and the laser energy absorbed at each incidence were computed. The material parameters were taken from [37,43–46] to model Ti-6Al-4V. Details of the physics models, materials parameters, and numerical procedures are described below.

Metal laser melting is a complex phenomenon involving the coupling of phase transitions (melting and solidification), flow of MP and vapor, laser energy reflection and absorption, and thermal transport. To address such complex system, we have developed a three-dimensional fully-coupled phase-field, fluid dynamics, and ray tracing model. The Lattice Boltzmann Method was implemented to model MP hydrodynamics, while phase-field modeling was applied for solid-liquid phase transitions. Thermal diffusion, radiation, surface convection, latent heat, laser energy and laser ray tracing were included and implemented in the thermal equations. Ray tracing was implemented as geometrical ray absorption and reflection at the solid or liquid / vapor interface.

2.1. Lattice Boltzmann method formulation

The Lattice Boltzmann Method (LBM) was chosen to model fluid dynamics because of its high efficiency in parallel numerical calculations, as well as its compatibility with the typical dense grid of phase field formulations. Our model is based on the early work by Fakhari et al. [42]. The lattice Boltzmann equation (LBE) for hydrodynamics is defined by Eqs. (1–7).

$$g_\alpha(\vec{x}+\vec{e}_\alpha\delta t, t+\delta t) = g_\alpha(\vec{x},t) + \Omega_\alpha(\vec{x},t) + F_\alpha(\vec{x},t) \tag{1}$$

$$\Omega_\alpha^{BGK} = -\frac{g_\alpha - g_\alpha^{eq} + 0.5F_\alpha}{\tau + 0.5} \tag{2}$$

$$F_\alpha(\vec{x},t) = \delta t w_a \frac{\vec{e}_\alpha \bullet \vec{F}_{external}}{\rho c_s^2} \tag{3}$$

$$g_\alpha^{eq} = w_a\left[p^* + \frac{\vec{e}_\alpha \bullet \vec{u}}{c_s^2} + \frac{(\vec{e}_\alpha \bullet \vec{u})^2}{2c_s^4} - \frac{\vec{u}\bullet\vec{u}}{2c_s^2}\right] \tag{4}$$

$$\tau_{LBM} = \mu/\rho c_s^2 \tag{5}$$

$$\rho = \rho_s\phi_s + \rho_l\phi_l + \rho_v\phi_v \tag{6}$$

$$p^* = \sum_\alpha g_\alpha,\ \vec{u} = \sum_\alpha g_\alpha \vec{e}_\alpha + \frac{\vec{F}_{external}}{2\rho}\delta t \tag{7}$$

In these equations, subscript α represents a direction in space. The vector $\vec{e}_\alpha$ is the mesoscopic velocity. The velocity-based distribution function for incompressible fluids is g_α, together with its modified equilibrium distribution g_α^{eq} given by Eq. (3). Ω_α is the collision term, and the single-relaxation-time (SRT) formulation was used, as shown in Eq. (2). Such choice was justified by the fact that fluid flow in the melt pool was laminar. In fact, for a typical metal liquid with a density of ~9000 Kg/m^3, a fluid velocity of ~1 m/s, a melt pool size ~500 μm, and a viscosity of $6\bullet10^{-3}$ Pa•s, the Reynolds number is ~700, which is comfortably within the domain of laminar flow (Re < 2000) [52]. $\vec{F}_{external}$ and F_α are the external force and hydrodynamic force, respectively. τ_{LBM} is the relaxation time, ρ is the density, μ is the viscosity, c_s is the sound speed for an ideal fluid, and for the D3Q15 lattice, $c_s = \sqrt{3}/3$. The terms ϕ_s, ϕ_l and ϕ_v are the phase order parameters of solid, liquid MP and vapor, respectively. The term $p^* = p/\rho c_s^2$ is the normalized pressure. Eq. (7) is consistent to the zeroth and first moments of the distribution function. The density ratio of liquid over vapor was 1000. At each interface, the physical properties of the mixture, e.g. density, viscosity, thermal conductivity, specific heat capacity, are treated as a linear interpolation of the two phases, as described by Eq. (6). The D3Q15 lattice [27] was used with $w_0 = 2/9$, $w_{1-6} = 1/9$, $w_{7-15} = 1/72$.

In our model, the phase interface is governed by the phase field formulation rather than the LBE for interface tracking; the role of hydrodynamics is to calculate the velocity and pressure fields. Further, we have included the model improvements following Sun's work [26] related to the calculation of external forces. The forces are listed in Eqs. (8–12).

$$\vec{F}_{external} = \frac{2\rho}{\rho_v + \rho_l}(\vec{F}_s + \vec{F}_{recoil} + \vec{F}_{Marangini} + \rho\vec{g}) \tag{8}$$

$$\vec{F}_s = \mu_\phi \nabla\phi \tag{9}$$

$$\mu_\phi = 4\beta\phi(\phi-0.5)(\phi-1) - \kappa\nabla^2\phi \tag{10}$$

$$\vec{F}_{recoil} = 0.54[p_0 \exp\left(\frac{\Delta H_{evap}}{R_v T_v}\frac{T-T_v}{T}\right) - p_0]\bullet\vec{n} \tag{11}$$

$$\vec{F}_{Marangoni} = [\nabla T - (\vec{n}\bullet\nabla T)\bullet\vec{n}]\frac{d\sigma}{dT} \tag{12}$$

In these equations, $\vec{F}_s$ is the surface tension force at liquid/vapor interface. The term μ_ϕ is the chemical potential. The terms β and κ are related to the surface tension σ and interface thickness η by $\beta = 12\sigma/\eta$ and $\kappa = 3\sigma\eta/2$. Only the hydrodynamics of liquid and vapor are calculated, therefore ϕ equals to ϕ_l, while at the triple junctions, ϕ equals to $\phi_l+\phi_s$. Bounce-back boundary conditions were applied in the LBM calculations. The term p_0 is the ambient pressure, ΔH_{evap} is the evaporation latent heat, R_V is the gas constant, and $\vec{n}$ is the vector normal to the interface. Recoil pressure is calculated where saturated vapor pressure is above ambient pressure p_0 [47].

2.2. Phase-field formulation

Vapor was treated as a conserved phase and did not undergo phase transitions. Although evaporation was not modeled directly, the recoil pressure was taken into account in melt flow while the evaporation latent heat was included in thermal transport. Because our focus was to model the keyhole and the vapor/liquid interface, the solid/liquid transition was modeled with a single temperature for simplicity, without including the mushy zone.

The total free energy F in the model is given by

$$F = \int_\Omega dx\{\quad f_{inter}+f_{chem}\quad\} \tag{13}$$

$$f_{inter} = \sum_{i=s,\ l}\frac{\kappa}{2}|\nabla\phi_i|^2 + \beta\phi_i^2(1-\phi_i)^2 \tag{14}$$

$$f_{phase} = g_{phase}\left[\left[(\phi_s+\phi_v-1)^2+\phi_l^2\right]\theta(\tau)+\left[(\phi_l+\phi_v-1)^2+\phi_s^2\right](1-\theta(\tau))\right] \tag{15}$$

$$\frac{\partial\phi_s}{\partial t} = -M_s\frac{\delta F}{\delta\phi_s} \tag{16}$$

$$\frac{\partial\phi_l}{\partial t} + \vec{u}\bullet\nabla\phi_l = -M_l\frac{\delta F}{\delta\phi_l} \tag{17}$$

$$\frac{\partial\phi_v}{\partial t} + \vec{u}\bullet\nabla\phi_v = \nabla M_v\nabla\frac{\delta F}{\delta\phi_v} \tag{18}$$

where f_{inter} is the interfacial energy with a double-well potential,κ is the gradient energy coefficient and β is the potential coefficient, which are consistent with Eq. (10). In the simulation, solid, liquid and vapor are assumed to share the same surface tension with vapor. The term f_{phase} is the energy for phase transition where $\tau = T/T_m$, $\theta(\tau)\to1$ when $\tau<1$ and $\theta(\tau)\to0$ when $\tau>1$ [37]. This formula ensures that the energy reaches its minimum at ($\phi_s = 1-\phi_v$, $\phi_l = 0$) when T is below T_m and ($\phi_s = 0$, $\phi_l = 1-\phi_v$) when T is above T_m. The term g_{phase} is the chemical driving force and is designed as a linear relation with undercooling/overheating, i.e. $|T-T_m|$, for pure solid/liquid transition. $M = M_0\exp(-\Delta G_m/RT)$ is the temperature-dependent interfacial mobility, where ΔG_m is the activation energy. The governing equations for time-dependent interface evolution are described in Eqs. (17 and 18).

2.3. Thermal transport

The governing equation implemented for thermal transport in this work is Eq. (19). The terms from left to right are temperature variation, flow flux, diffusion flux, laser heat, evaporation latent heat and solid/liquid transition latent heat, respectively. Eq. (20) describes the in-plane laser energy with Gaussian distribution.

$$\rho c_p\left(\frac{\partial T}{\partial t}+\vec{u}\bullet\nabla T\right) = \nabla k_T\nabla T + Q_{laser} - Q_{evap} - Q_{ls} \tag{19}$$

$$Q_{laser} = q_{max}exp(-\frac{2r^2}{R^2})\alpha(\vec{r}) \tag{20}$$

$$Q_{ls} = \rho d\phi_{ls}\Delta H_{ls} \tag{21}$$

$$-\vec{n}\bullet\vec{q} = -h_T(T-T_0) - e_T\sigma_T(T^4-T_0^4) \tag{22}$$

$$Q_{1,laser}^{hat} = q_{max} \tag{23}$$

where c_p is the heat capacity, $\vec{u}$ is the flow velocity, k_T is heat conductivity, h_T is convective heat transfer coefficient, e_T is emissivity, σ_T is Stefan-Boltzmann constant, T_0, T_m, and T_v are the ambient temperature, melting point and boiling temperatures, respectively. Further, Q_{evap} is the total evaporation latent heat, and Q_{ls} is the total melting/solidification latent heat. ΔH_{lv} is the molar evaporation latent heat and ΔH_{ls} is the molar melting/solidification latent heat. Q_{laser} is the absorbed laser energy, and $\alpha(\vec{r})$ is the absorption rate depending on geometry, refractive indices of the material, and the laser incident angle. In this work, the absorption rate is calculated by ray tracing method, where multiple reflections are considered. a_{evap} is a numerical parameter to adjust the total evaporation thermal flux. The heat losses from surface convection and radiation were calculated as shown by Eq. (22). Eq. (23) is the model for an ideal flat-hat laser.

2.4. Ray-tracing formulation

The energy absorption of laser beam is modelled using the ray-tracing method. The basic process of this method is tracking the laser light reflection from surface to surface, and at the same time, computing the energy absorption when each reflection happens. To elaborate, the metal material is represented by an arbitrary surface, which consists of many finite sized triangular or rectangular plane surfaces, i.e. meshes. The laser beam is represented by a bundle of rays. Each ray has features of a starting point, incident direction, energy, wavelength and polarization. Intersection tests are performed between each ray and all meshes (surfaces). The ray-mesh intersections can be treated as line-plane intersections, based on geometric optics. If an intersection occurs, absorption and reflection, including absorptivity, propagation direction, and remaining energy of each ray, are calculated between the ray and the geometry, taking into account the incidence angle, polarization for each incidence angle, and the optical parameters of the material. The calculation is based on Fresnel Eqs. (24 and 25) [48].

$$R_p = \left|\frac{n_1 cos\theta_t - n_2 cos\theta_i}{n_1 cos\theta_t + n_2 cos\theta_i}\right|^2 \tag{24}$$

$$R_s = \left|\frac{n_1 cos\theta_i - n_2 cos\theta_t}{n_1 cos\theta_i + n_2 cos\theta_t}\right|^2 \tag{25}$$

These equations describe the reflectivity, which is the ratio of energy reflected by the material, when the light is incident from medium 1 to medium 2. The terms R_p and R_s are the reflectivity for p- and s- polarized laser, respectively. The terms $n1$, $n2$ are the refractive index of medium 1 and 2. In this work, light is assumed to be incident from the ambient gas to the metal target. For this reason, $n_1 = 1$ is chosen as a fairly good approximation. On the other hand, n_2 is the refractive index of the metal substrate. The values $\theta_t = \sqrt{1-\left(\frac{n_1}{n_2}sin\theta_i\right)^2}$ are the incident and transmitted angles, respectively. For a light-metal interaction, light is

reflected and absorbed. Absorptivity, which is defined as the ratio of light energy absorbed by the material, is therefore calculated as in Eqs. (26 and 27):

$$A_p = 1 - R_p \tag{26}$$

$$A_s = 1 - R_s \tag{27}$$

where A_p and A_s are the absorptivity for p- and s- polarized laser, respectively. After a reflection, the features of each ray are updated with remaining energy, starting point, and direction. If no intersection happens, the ray propagates out of the simulation space, and is deleted from the simulation. The intersection tests for all rays are repeated until all the rays propagate out of the simulation space, or their energies are below a threshold value and therefore can be ignored. During the simulation, the ray-tracing scheme computed the energy absorbed by the material at each ray point of incidence on the material, including multiple reflections. When the resolution of the laser was high enough, i.e. the ray size is small enough, we were able to obtain the laser energy absorbed by any geometry of the material. The total absorbed energy was the sum of all absorption points. Finally, the absorptivity was the ratio of the absorbed energy to the laser beam energy, and was thus, a scalar between 0 and 1.

2.5. Simulation parameters

All physical parameters of Ti-6Al-4 V applied in the simulation are listed in Table 1. The density ratio of the condensed state and vapor is 1000, the viscosity ratios among solid, liquid and vapor are assumed to be 10^6:1: 10^{-3}. The value of ε_T is chosen as 0.18 in order to obtain an initial laser absorptivity of 0.3 [49]. The ambient temperature is 300 K and the temperature upper limit is set to 4100 K, which is about 800 K above boiling point, to match the experimental time scale for the transition from the stable to the keyhole regime. The thermal conductivity and specific heat data of pure argon is adopted as the initial vapor data.

The simulation box for all the cases was 500 μm × 500 μm × 500 μm, and the height of the substrate was 425 μm. The density, length, time, and temperature were non-dimensionalized by 4400 Kg/m^3, 2.5 ×10^{-6} m, 5.0 ×10^{-8} s and 1.0 K, respectively. The thickness of the diffuse interface was 5 grid points. The cases with laser power of more than 300 W required a smaller time step of 2.5 ×10^{-8} s, whereas in all other cases, the time step was 5.0 ×10^{-8} s. Capping limit for spurious flow velocities was set to 0.1 to avoid numerical divergences. The convergence of the PF, LBM and thermal calculations with different values of grid size and time step was checked. The combination of time step and grid size applied in this work was chosen from those combinations that ensured stable and consistent simulation results while offering high resolution for the keyhole and melt pool profiles.

Table 1
Thermophysical parameters of Ti-6Al-4V parameters in the simulation.

Property	Value	Reference	Property	Value	Reference
$\rho_{s/l}$	4400 Kg/m^3	[40]	T_m	1928 K	[40]
μ_l	5 × 10^3 Pa·s	[40]	T_v	3315 K	[40]
p_0	101,325 Pa		$c_{p,s}$	750 J/Kg/k	[39]
σ	1.5 N/m	[40]	$c_{p,l}$	930 J/Kg/k	[39]
γ	-2.6 × 10^{-4} N/m/K	[40]	$c_{p,v}$	520 J/Kg/k	
ΔH_{sl}	286 KJ/Kg	[40]	$k_{T,s}$	13 W/m/K	[39]
ΔH_{lv}	9.7 MJ/Kg	[40]	$k_{T,l}$	48 W/m/K	[37]
R_V	195 J/Kg/K	[40]	$k_{T,v}$	0.018 W/m/K	
h_T	25 W/m^2/K	[40]	ε_T	0.18	
g	10 m/s^2		G_m	2.5 ×10^5 J/mol/K	[50]
$M_{0,sl}$	6 ×10^6 m^3/s/J	[50]	$M_{0,v}$	7 × 10^2 Kg^3/m/s/J	[50]
T_0	300 K				

3. Results and discussions

3.1. Mechanisms of five regimes in keyhole dynamics

We first report our modelling predictions on a typical experimental setting of Cunningham et al. [16], in which the laser spot size was 140 μm and the laser power was 156 W. In this setting, the stationary laser was vertically shined on a Ti-6Al-4V bare plate. Snapshots of the time evolution of MP formation and evolution for the typical case are shown in Fig. 1, in which Fig. 1A-F show the experimental observations of the MP from [16], Fig. 1A'-F' show our simulation results of the MP with ray-tracing trajectories and temperature contours, and Fig. 1A''-F'' show the simulation results of the MP with the liquid flow velocity field. In addition, the variation of the keyhole depth with the laser shining time is shown in Fig. 1G (the red curve for the experiment result and the blue curve for the modelling result). The modelling results shown in Fig. 1A′-F′, Fig. 1A''-F′ and G clearly demonstrate the five regimes in the formation and evolution of the MP: (i) melting (Fig. 1A′-A''), (ii) vapor depression formation and growth (Fig. 1B′-B''), (iii) vapor depression instability (Fig. 1C′-C''), (iv) keyhole formation and growth (Fig. 1D′-D''), and (v) complex MP shape change (Fig. 1E′-E'' and F′-F''), which match with the experimental observations shown in Fig. 1A-F, G and the Movie S1 of keyhole dynamics in the supplementary materials in [16] almost exactly, thus validating our modelling procedure.

Supplementary material related to this article can be found online at doi:10.1016/j.addma.2022.102779.

In the following, we analyze and discuss the underlying dynamics of the MP and keyhole and their controlling physical factors in each of these regimes. To reveal the underlying controlling factors, we have also calculated the variations of the highest temperature of the MP, laser energy absorptivity, the recoil pressure force and the surface tension force, and the results are shown in Fig. 1H and I.

In Regime (i), once the laser was turned on, a MP started to form due to the rise of temperature as shown in Fig. 1H (the black curve). In this regime, the recoiling pressure force and surface tension forces are both negligible, and the MP surface is essentially flat.

Regime (ii) started when temperature exceeded the boiling point. In this regime, the laser energy absorptivity increased slowly and linearly (the red curve), and the highest MP temperature reached a plateau at about 3500 K (the black curve) as shown in Fig. 1H. At this high temperature, the vaporization started, giving rise to the recoil pressure on the MP surface (the black curve), which was balanced by the rise of the surface tension due to increased local curvature (the blue curve) as shown in Fig. 1I. As a result, a vapor depression was formed and then grew steadily as shown in Fig. 1B′ and G (the blue curve). Interestingly, there was a small oscillation of the vapor depression as evidenced by the fluctuations of the keyhole depth as shown in the inset G′ in Fig. 1G. At this stage, due to the presence of temperature gradient on the MP surface, the Marangoni force on the liquid surface provided the main driving force for the melt flow (Fig. 1B''). Fluid velocity was sustained by the continuous action of the Marangoni force, which was driven by the local temperature gradient, as shown in Fig. 1C''. The accelerated circulation was able to bring more heat to the solid/liquid boundary, causing the enlargement (widening and deepening) of the MP, and the growth of the MP and vapor depression.

When keyhole depth reached a critical depth, the vapor depression became instable, that is, Regime (iii). The instability corresponds to the turning point highlighted in the time vs the depth curve (the blue curve) in Fig. 1G. The physical origin underlying the instability is that the recoil pressure force (the black curve) increased drastically as marked by the red arrow in Fig. 1I, which was not able to be balanced by the surface tension surface force (the blue curve in Fig. 1I). Hence it was the unbalanced resultant force that caused the vapor depression to lose instability.

The vapor depression instability marks the beginning of the keyhole formation and growth, that is, Regime (iv). There are several interesting

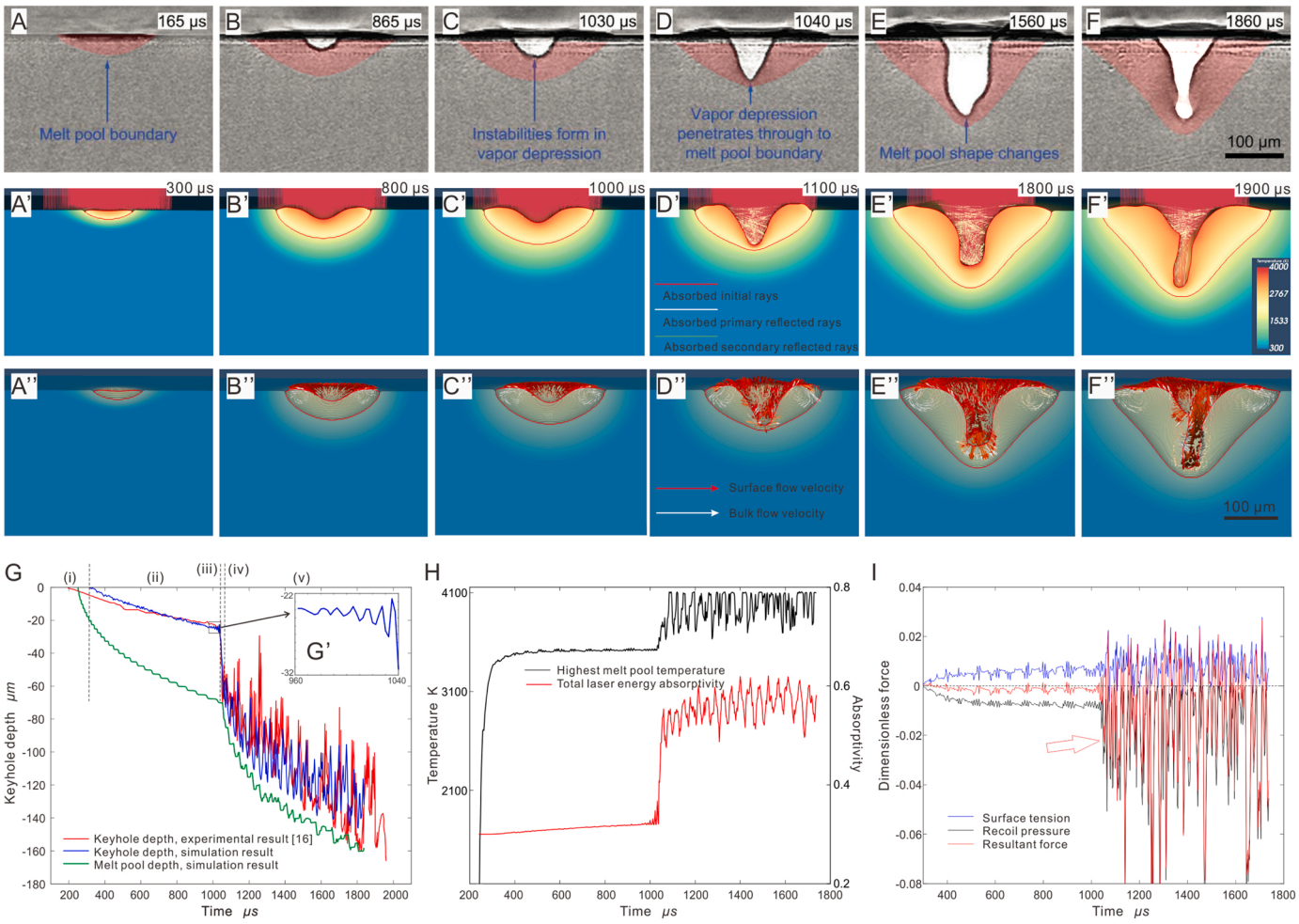

Fig. 1. The evolution of keyhole and MP of Ti-6Al-4 V alloy under stationary laser beam. The laser power is 156 W and the laser spot size is 140 μm. (A-F) In-situ ultrahigh speed X-ray imaging results [16]. The original order of subfigures in [16] was adjusted according to the design of this work. The light red regions denote the MP, and the white regions denote the vapor depression or keyhole. (A'-F') Longitudinal section of the simulation results with laser ray tracing. Red lines denote the primary laser rays, while the white and light green lines denote the captured first and second reflected rays. The figures also show the phase interface and temperature distribution. In the simulation, laser was turned on at 200 μs. (A''-F'') Longitudinal section of the simulation results with the liquid flow velocity field. Red arrows denote the flow velocity of the MP surface and white arrows denote the internal flows. (G) The dynamics of MP depth and keyhole depth. The red line denotes the experimental result of the keyhole depth [16], the blue line and the green line denote the keyhole depth and MP depth in simulation, respectively. The keyhole dynamics near the critical depth is showed in (G'). (H) The evolution of highest MP temperature (black line) and total laser energy absorptivity (red line). (I) The evolution of surface tension force (blue line) and recoil pressure force (black line) at the center point of the MP surface along the vertical direction. A positive value means the force is pointing upwards. Five regimes [16] of the dynamics, that is, (i) melting, (ii) vapor depression formation and stable growth, (iii) instability toward keyhole formation, (iv) keyhole formation and growth, (v) complex keyhole shape, are marked in (G). (A'-C') show the process of melting (Regime (i)) and stable vapor depression formation and growth (Regime (ii)). The main driving force for the melt flow is the Marangoni force. Circulation can be seen in (C'') near the MP / substrate boundaries. When the Marangoni force-driven surface flow hits the unmelt solid substrate, the bounced-back flow forms circulations. In this process, highest MP temperature rises from the ambient temperature and keeps balanced at near 3500 K. (G') shows the vapor depression instability (Regime (iii)) when the keyhole depth reaches the critical depth. The instability influences the total absorbed laser energy through the absorption of reflected rays, which results in the change of the MP temperature and temperature-dependent recoil pressure further, as shown in (H) and (I). (D') shows the keyhole formation and growth (Regime (iv)) driven by the recoil pressure. Once the surface tension cannot balance the sharp increase of the recoil pressure, as marked by the black arrow in (I), Regime (iii) will transform to Regime (iv). (G) also shows that at the end of the keyhole growth, the keyhole tip is approaching the MP bottom (the green line), and as a result, the keyhole growth is limited by the MP depth. (E') and (F') show irregular, violent keyhole oscillations with complex keyhole morphology (Regime (v)).
Adapted with permission from Ref [16]. Copyright 2019 American Association for the Advancement of Science.

changes associated with the keyhole formation and growth. First, there was a sharp increase in the growth velocity of the vapor depression as shown in Fig. 1D' and D'', causing a drastic increase in the keyhole depth/width ratio shown in the blue curve in Fig. 2C. Second, there was a sharp rise in the highest MP temperature as shown in Fig. 1H (the black curve), which was due to the increase in the laser energy absorption from initial 0.3–0.55 as shown in Fig. 1H (the red curve), which was due to the increased trapping of laser rays (multiple laser reflections and absorptions) as shown in the white and light green lines of Fig. 1D', which is in contrast to the scenarios of Fig. 1(A'-C'), where the laser rays were absorbed only once and then reflected out of the surface. Lastly, the recoil pressure force in this regime always outpaced the surface tension force, and this unbalanced resultant force drove the keyhole formation and growth, that is, Regime (iv), which is consistent with the study of Mayi et al. [51]. Hence, Regime (iv) involves the coupling of a few factors, such as the surface geometry, temperature, recoil pressure, surface tension, laser energy absorption, highlighting the complexity in the keyhole formation and growth processes.

Right after the keyhole was formed, it is seen from Fig. 1D'-D'' that the keyhole tip quickly approached the MP bottom. When the contact

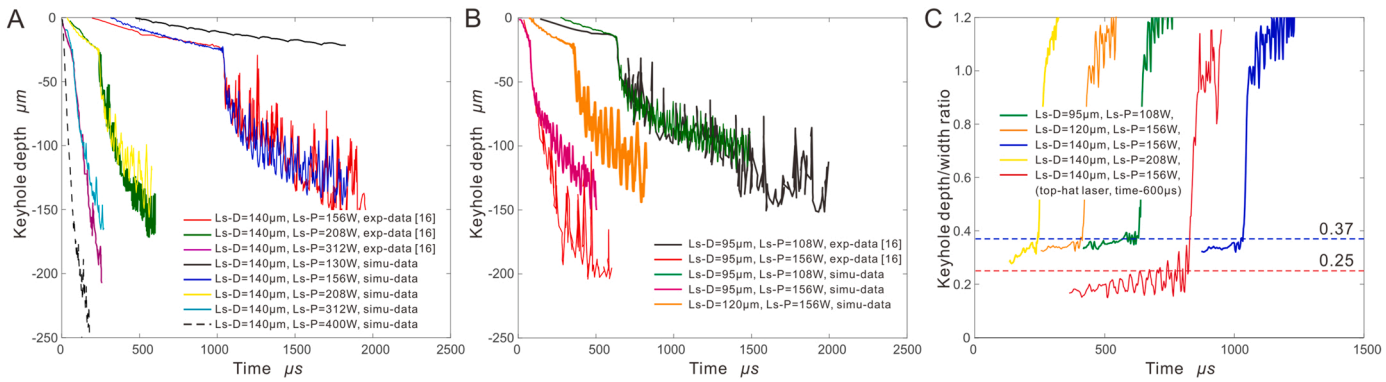

Fig. 2. Keyhole depth evolution during stationary laser melting. (A) At the laser spot size of 140 μm, instability occurs only at a certain laser power range. If the laser power is too low, for example, at 130 W, the vapor depression maintains a stable growth up to 2000 μs. The turning point also disappears if the laser power is large enough, for example, at 400 W. For a laser spot size of 140 μm, the laser power range that has the turning point is in between 139 W and 400 W. (B) At laser spot sizes of 95 μm and 120 μm. The critical depths for the keyhole formation with the same laser spot size are almost the same, but are deeper for larger laser spot sizes. (C) The evolution of keyhole depth/width ratio. The ratio of the simulation results with Gaussian type laser is about 0.37, while the ratio with top-hat laser is 0.25.

occurred, the MP bottom, which was also the substrate surface, was able to bounce the keyhole upward. However, the recoil pressure force continued to push the keyhole downward. As a result, there was a violent oscillation of the keyhole tip as shown in Fig. 1G (the blue curve). It should be noted that when the MP grew deeper, the keyhole also grew, but the keyhole growth was limited by the growth of the MP (green curve in Fig. 1G).

When the MP grew deeper and deeper, the keyhole became much elongated. In this condition, the slightest loss of keyhole geometrical axisymmetry induced a highly non-uniform laser energy absorption on the keyhole side surface, leading to non-uniform heating of the keyhole surface and to non-uniform recoil pressure on the keyhole side surface, which triggered Regime (v). The non-uniform recoil pressure on the keyhole side surface caused an irregular, violent oscillation of the keyhole shape as shown in Fig. 1F′-F′′, which could induce bubble spillover (More detailed discussion of this will be given later).

3.2. Influence of laser power and laser spot size

Orthogonal simulations of other laser spot sizes and laser powers were also performed and the results of the evolution of keyhole depth are shown in Fig. 2. These simulation results reveal two interesting observations. First, the critical vapor depression depth that marks the vapor depression instability is almost the same for different laser powers with same laser spot size, while it varies with laser spot sizes. This can be seen in Fig. 2A, where the critical depth is about 17 μm for a laser spot size of 95 μm and laser powers of 108 W and 156 W, and it is about 25 μm for laser spot size of 140 μm and laser powers of 156 W, 208 W and 312 W. As shown in Fig. 2B, the critical depths for the laser spot sizes of 95 μm, 120 μm and 140 μm are about 17 μm, 21 μm and 25 μm, respectively. These results imply that the laser spot size is roughly 5.6 times of the critical depth under these conditions. Second, the typical MP evolution pathway, as shown in Fig. 1, can be altered by a proper choice of combination of laser power and spot size. To demonstrate this, we performed a series of simulations with different laser powers while keeping other system parameters unchanged, and the variations of the keyhole depth with the laser shining time are shown in Fig. 2A. It is seen that on the one hand, when the power is too low, e.g., at 130 W, the vapor depression grows slowly, the vapor depression depth cannot reach the critical depth and thus there is no keyhole formation up to 2000 μs. On the other hand, if the laser power is too high, e.g., at 400 W, the keyhole growth front almost coincides with the MP growth front, and the MP depth grows sharply and yet relatively smoothly, while the keyhole depth also grows sharply with the same trend, but with moderate oscillations.

We would like to highlight that the keyhole formation and growth is a complex coupling process involving a few physical quantities including the geometry of the vapor depression, surface temperature, surface tension, recoil pressure, and laser energy absorption. The laser energy absorption causes a rise of temperature at the MP surface. When the temperature reaches the vaporization temperature, the vaporization induces a recoil pressure on the surface, causing the formation of MP surface depression. When the vapor depression depth/width ratio reaches a critical level, multiple laser ray reflections/absorptions occur, causing a drastic increase in the laser energy absorption, which in turn causes the sharp rise of surface temperature. This rise in temperature drastically increases in the recoil pressure, which in turn causes an even larger depression depth/width ratio. It is this positive-feedback coupling of multiple physical quantities that leads to the runaway process, which breaks the stable vapor depression growth and thus leads to the keyhole formation.

Since the absorption of multiple reflected rays is related to the keyhole geometry, we now turn our attention to the critical depth for the transition from the single ray reflection to multiple ray reflections. We calculated the geometrical ratios of the keyhole depth and width at different laser spot sizes, and the results are plotted in Fig. 2C. It is seen that for a Gaussian laser energy distribution, this threshold geometrical ratio is about 0.37, while for a top-hat energy distribution, it is about 0.25. Clearly, there is no universal threshold geometrical ratio as different laser energy distributions show different threshold ratios. These ratios could be used as guidelines to control/maintain the melt pool within the stable regime, for improving the part quality in processes including selective laser melting, laser shock peening and laser cladding.

3.3. Four types of keyhole oscillation

Remarkably, our high-fidelity simulations also reveal four different types of oscillations during the MP growth. The first one (Type (a)), the melt flow-induced oscillation, occurs in Regime (ii), the second one (Type (b)), the recoil pressure-driven oscillation, occurs in Regime (iii), the third one (Type (c)), oscillation driven by both the recoil pressure and the bouncing force from the MP bottom after Regime (iv) and the last one (Type (d)), the irregular, violent oscillation, occurs in Regime (v). There four different oscillations are driven by different physical forces and show different oscillation characteristics. Below, we discuss these four different oscillations and their mechanisms in details.

We begin by discussing Type (a), i.e., the melt flow-induced oscillation. As shown in Figs. 2 and 3A(a), even during the stable vapor depression growth (that is, Regime (ii)) in the typical case discussed, the vapor depression already shows an oscillation. It is noted that the

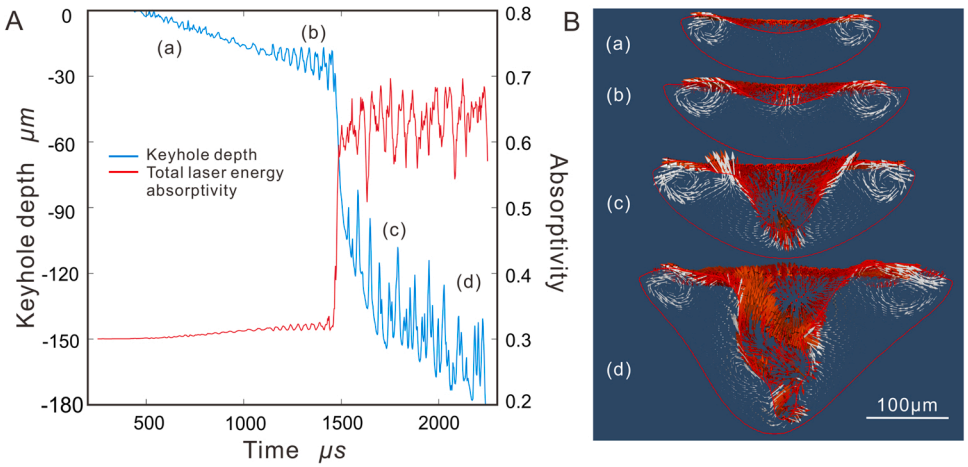

Fig. 3. Time evolution of keyhole depth and laser absorptivity and snapshots for the melt flow for four different types of oscillations. (A) Time evolution of the keyhole depth and laser absorptivity. (In order to be consistent with Fig. 1, the laser was turned on at 200 μs) (B) Four types of keyhole oscillations and mechanisms: (a) melt flow-induced oscillation, (b) recoil pressure-driven regular oscillation, (c) MP bottom bouncing back oscillation, and (d) recoil pressure-driven irregular oscillation. In the simulation, the top-hat laser spot size is 140 μm and the laser power is 156 W.

amplitude of this oscillation is very small compared to the MP depth. The mechanism for the melt flow-induced oscillation is illustrated in Fig. 3B(a). Because of the temperature gradient at the MP surface, the surface always has a flow from the center to the sides of the MP driven by the Marangoni force. The flow is bounced back when it hits the unmelt solid substrate, and circulations are formed near the liquid/solid boundaries. The bounced-back flow influences the balance between surface tension and recoil pressure of the surface, as shown in Fig. 1I, and this induces a slight oscillation. In this type of oscillation, the Marangoni force plays the dominant role while the recoil pressure force is relatively stable and plays a negligible role.

Type (b) oscillation is driven by the recoil pressure. This oscillation, which is shown in Fig. 3A(b) and (b), occurs when the vapor depression depth was close to the critical depth, and was in fact observed in a previous in-situ X-ray imaging study (see the Movie S1 in the supplementary materials of Cunningham et al. in [16]). Our simulation under the same conditions (laser power of 156 W and laser size of 140 μm) captured this oscillation and the result is shown in Fig. 1G′. Moreover, as shown in Fig. 3A, this type of oscillation is more obvious in the melting process of top-hat laser. Although the amplitude of Type (b) oscillation is relatively small, its oscillation can become important near the critical depth by affecting the laser reflection. More specifically, the Type (b) oscillation near the critical depth leads to the laser energy absorption oscillation, which in turn causes the oscillation of surface temperature and recoil pressure. When the amplitude of Type (b) oscillation is too large and across the critical depth, the instability occurs, leading to the formation of keyhole. The oscillation of the laser energy absorptivity before the critical point is evidenced in Fig. 3A. A rising process of Type (b) oscillation is shown in Fig. 3B(b).

Next, we discuss Type (c) oscillation as shown in Fig. 3A(c) and (c). As shown in Fig. 1G, this oscillation occurs right after the keyhole formation. When the fast-growing keyhole tip was approaching the MP bottom, the substrate at the MP bottom bounced the keyhole upward, while the recoil pressure continued to push the keyhole tip downward. These up and down processes repeated themselves, leading to the Type (c) oscillation. There are several interesting characteristics associated with this oscillation. First, the highest temperature of the MP fluctuates around a constant value, while the laser energy absorptivity increases slowly also with small fluctuations. Second, by comparing the MP depth and the down oscillation peak envelope, we see that the depth of the MP and keyhole not only follows the same trend, the MP bottom and the down peak envelope are also close to each other. This suggests that the MP bottom limits the downward motion of the keyhole and the average keyhole downward speed essentially follows the MP downward speed. By inspecting Fig. 1I, we notice the absolute value of recoil pressure increases after the turning point and decreases after a peak. While the keyhole grows deeper, the surface tension force increases as the curvature increases. The resultant force drives the keyhole tip back, causing the relatively regular and yet violent oscillation.

Lastly, we discuss Type (d) oscillation, that is, the irregular, violent oscillation. As shown in Fig. 1G and Fig. 3A(d), after the MP grows deeper, the keyhole becomes much elongated. This leads to a complex, irregular, violent oscillation of the keyhole in Regime (v). The complex shape of the keyhole indicates that the keyhole has lost its axisymmetry as shown in Fig. 3B(d). As a result, the laser energy absorption at the keyhole side surface becomes highly non-uniform, and thus the temperature distribution also becomes highly non-uniform, which in turn leads to a strongly non-uniform distribution of the recoil pressure force at the side surface of the keyhole. Consequently, the MP enters a state that is highly dynamic. In this regime, the highly non-uniform recoil pressure on the side surface, the recoil pressure on the bottom surface of the keyhole and the MP bottom bouncing force are all active at the same time, and play important roles in the violent oscillations.

It is noted that the first two types of oscillations occur in Regime (ii) while the latter two types of oscillations occur in Regime (v). Our analyses have shown that for different laser melting processes, different types of oscillations can be present. For example, if the laser power is large enough (e.g., for the laser power of above 400 W in Fig. 2A), the recoil pressure always plays a dominant role and the keyhole reaches Regime (v) sharply. As a result, only Type (d) oscillations are present. This is consistent with the previous studies of keyhole dynamics under high laser powers [9,26]. On the other hand, if the laser power is too low, the vapor depression is unable to reach the threshold geometrical ratio (e.g., for the laser power of 130 W in Fig. 2A), only Type (a) oscillation is present. For a laser power in between (e.g., the laser power of 156 W in Fig. 2A), all the four types of oscillations can occur.

3.4. Bubble formation

A keyhole may experience a variety of complex morphologies during the Type (d) oscillation. Our simulations, as shown in Fig. 4, explicitly demonstrate that when the surface of the MP becomes sufficiently irregular, spillover of bubbles from the keyhole tip may occur under additive manufacturing process parameter values. Fig. 4 shows the snapshots of the spill-over of a bubble during the violent oscillation. Fig. 4(A-C) show the longitudinal section views of the melt flow, while Fig. 4(A′-C′) show the longitudinal section views of the MP morphology. It is seen from Fig. 4A′ that a vapor protrusion is formed at the bottom of the keyhole. As a result, laser rays are absorbed by the bottom surface of the protrusion. Such change in energy absorption increases the temperature-dependent recoil pressure on the bottom surface of the protrusion, which pushes the melt to flow along the normal direction of the bottom surface. The high flow velocity of the bottom surface of the protrusion is marked by the red arrows in Fig. 4(A). As a result, a high-

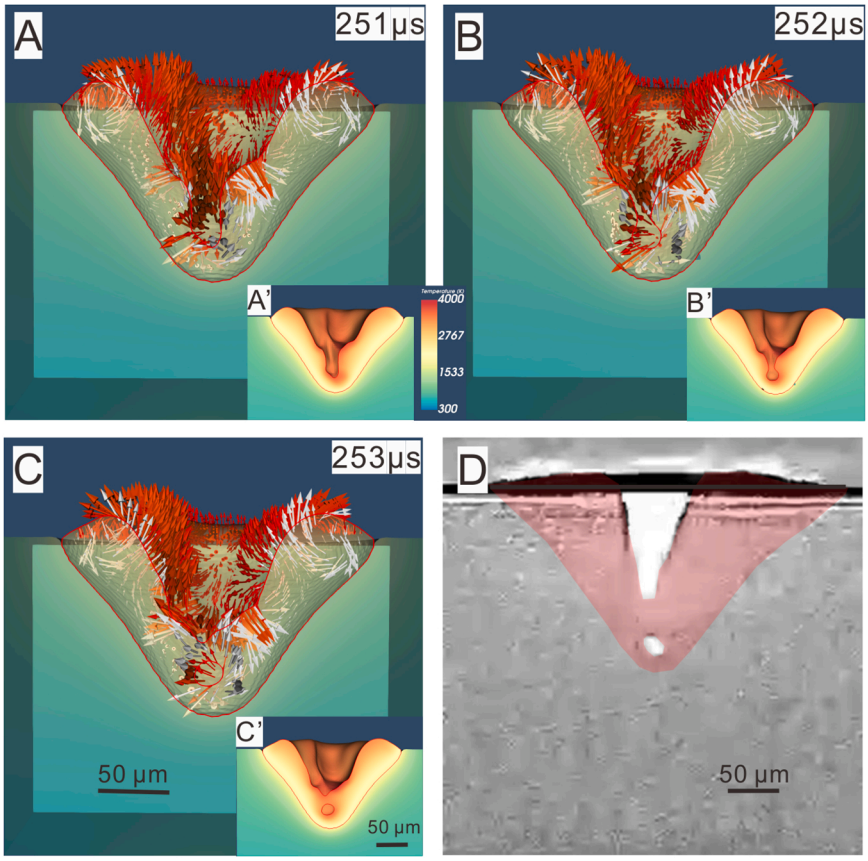

Fig. 4. The formation process of a bubble during the keyhole violent oscillation. (A-C) The longitudinal section views of the melt flow. (A′-C′) The longitudinal section views of the MP morphology. (A-B) and (A′-B′) show the process of bubble formation and (C) and (C′) show the bubble formation. In the simulation, the laser power is 156 W, the laser spot size is 100 μm , the substrate size is 300 μm × 300 μm × 225 μm, and the ambient temperature is set to 600 K based on the temperature contour in Fig. 1F′. (D) The in-situ X-ray observation of bubble formation [16]. Adapted with permission from Ref [16]. Copyright 2019 American Association for the Advancement of Science.

pressure region, in other words, a region, where the normalized fluid pressure is greater than 1, is formed at the bottom surface of the protrusion. As the protrusion becomes sufficiently elongated, an instability occurs at the middle of the protrusion, causing a necking along the horizontal plane of the protrusion. This necking instability is driven by the surface tension force that pinches the keyhole's sidewalls, leading to the spill-over of the bubble as shown in Fig. 4C. Our above findings are consistent with the in-situ X-ray observation of bubble formation [16] as shown in Fig. 4D. Clearly, the simulations demonstrate that the formation of vapor protrusions at the keyhole surface, and their associated changes in the laser energy absorption distribution plays an important role in the bubble spill-over process. Therefore, the time evolution of MP in Fig. 1G can also be described in terms of its oscillations: Melting → Type (a) oscillation → Type (b) oscillation → keyhole formation → Type (c) oscillation → Type (d) oscillation → bubble formation. While the present work focuses on stationary laser, it is natural to ask whether types (a)-(d) oscillation regimes are also found under moving laser. Such investigation will be the subject of a forthcoming work.

4. Conclusions

In summary, our physics-based modelling has allowed the quantitative prediction of the MP and keyhole evolutions during laser melting, as well as revelation of their underlying mechanisms and controlling factors. Beyond, we have identified four different types of oscillations in the MP and uncovered their underlying mechanisms and driving forces. We have also shown that under different laser powers, the melting processes can deviate from the typical cases. On one hand, if the laser power is too large, the recoil pressure plays a dominant role and the keyhole becomes highly distorted, facilitating the spillover of bubbles. On the other hand, if the laser power is too low, the vapor depression is unable to reach the threshold geometry to form keyhole. Hence, by changing the processing parameters, it is possible to control the dynamics of MPs and keyholes so as to improve the quality of additively manufactured and welded parts. The dynamics of MP and keyhole and their controlling factors revealed here provide new dimensions for controlling the laser-based additive manufacturing processes.

Funding

Singapore Agency for Science, Technology and Research (A*STAR) grant A19E1a0097 ("Industrial Digital Design and Additive Manufacturing Workflows"). Y-WZ acknowledges the support from Singapore A*STAR SERC CRF Award.

CRediT authorship contribution statement

Wei Ming: Writing – original draft, Methodology, Investigation. **Ding Wen Jun:** Writing – original draft, Software, Methodology. **Vastola Guglielmo:** Writing – original draft, Supervision, Project administration, Methodology, Investigation, Formal analysis, Conceptualization. **Zhang Yong-Wei:** Writing – review & editing, Writing – original draft, Supervision, Funding acquisition, Conceptualization.

MW performed the majority of the simulations and modellings with the help of WD, GV and YZ. WD coded the laser ray tracing part, GV designed the simulation platform and helped MW in implementing models, YZ is the supervisor and provided guidance and advice.

Declaration of Competing Interest

The authors declare that they have no known competing financial interests or personal relationships that could have appeared to influence the work reported in this paper.

Data Availability

All data needed to evaluate our conclusions are provided in the manuscript or the supplementary materials.

Acknowledgments

Early work by Liangxing Lu is gratefully acknowledged in porting the initial version of the code from two dimensions to three dimensions.

Appendix A. Supporting information

Supplementary data associated with this article can be found in the online version at doi:10.1016/j.addma.2022.102779.

References

[1] J.R. Lawrence, Advances in Laser Materials Processing: Technology, Research and Applications, second ed., Woodhead Publishing, 2017.
[2] W.M. Steen, Laser material processing—an overview, J. Opt. A Pure Appl. Opt. 5 (2003) S3–S7, https://doi.org/10.1088/1464-4258/5/4/351.
[3] Y.C. Shin, B. Wu, S. Lei, G.J. Cheng, Y.L. Yao, Overview of laser applications in manufacturing and materials processing in recent years, J. Manuf. Sci. Eng. 142 (11) (2020), 110818, https://doi.org/10.1115/1.4048397.
[4] V. Gunenthiram, P. Peyre, M. Schneider, M. Dal, F. Coste, I. Koutiri, R. Fabbro, Experimental analysis of spatter generation and melt-pool behavior during the powder bed laser beam melting process, J. Mater. Process. Technol. 251 (2018) 376–386, https://doi.org/10.1016/j.jmatprotec.2017.08.012.
[5] I. Yadroitsev, P. Bertrand, I. Smurov, Parametric analysis of the selective laser melting process, Appl. Surf. Sci. (2007) 8064–8069, https://doi.org/10.1016/j.apsusc.2007.02.088.
[6] Y. Zhang, G.S. Hong, D. Ye, K. Zhu, J.Y.H. Fuh, Extraction and evaluation of melt pool, plume and spatter information for powder-bed fusion AM process monitoring, Mater. Des. 156 (2018) 458–469, https://doi.org/10.1016/j.matdes.2018.07.002.
[7] E.A. Metzbower, Keyhole formation, Metall. Mater. Trans. B 24 (1993) 875–880, https://doi.org/10.1007/BF02663148.
[8] V. Semak, A. Matsunawa, The role of recoil pressure in energy balance during laser materials processing, J. Phys. D: Appl. Phys. 30 (18) (1997) 2541–2552, https://doi.org/10.1088/0022-3727/30/18/008.
[9] J.Y. Lee, S.H. Ko, D.F. Farson, C.D. Yoo, Mechanism of keyhole formation and stability in stationary laser welding, J. Phys. D Appl. Phys. 35 (2002) 1570–1576, https://doi.org/10.1088/0022-3727/35/13/320.
[10] J. Yin, D. Wang, L. Yang, H. Wei, P. Dong, L. Ke, G. Wang, H. Zhu, X. Zeng, Correlation between forming quality and spatter dynamics in laser powder bed fusion, Addit. Manuf. 31 (2020), 100958, https://doi.org/10.1016/j.addma.2019.100958.
[11] N. Kumar, S. Dash, A.K. Tyagi, B. Raj, Keyhole depth instability in case of CW CO_2 laser beam welding of mild steel, Sadhana 35 (2010) 609–618, https://doi.org/10.1007/s12046-010-0040-y.
[12] G. Zhang, B. Zhu, J. Zou, Q. Wu, R. Xiao, Correlation between the spatters and evaporation vapor on the front keyhole wall during fiber laser keyhole welding, J. Mater. Res. Tech. 9 (2020) 15143–15152, https://doi.org/10.1016/j.jmrt.2020.10.103.
[13] T. Klein, M. Vicanek, J. Kroos, I. Decker, G. Simon, Oscillations of the keyhole in penetration laser beam welding, J. Phys. D Appl. Phys. 27 (1994) 2023–2030, https://doi.org/10.1088/0022-3727/27/10/006.
[14] M. Courtois, M. Carin, P.L. Masson, S. Gaied, M. Balabane, A complete model of keyhole and MP dynamics to analyze instabilities and collapse during laser welding, J. Laser Appl. 26 (4) (2014), 042001, https://doi.org/10.2351/1.4886835.
[15] S. Pang, W. Chen, W. Wang, A quantitative model of keyhole instability induced porosity in laser welding of titanium alloy, Metall. Mater. Trans. A 45 (6) (2014) 2808–2818, https://doi.org/10.1007/s11661-014-2231-3.
[16] R. Cunningham, C. Zhao, N.D. Parab, C. Kantzos, J. Pauza, K. Fezzaa, T. Sun, A. D. Rollett, Keyhole threshold and morphology in laser melting revealed by ultrahigh-speed x-ray imaging, Science 363 (2019) 849–852, https://doi.org/10.1126/science.aav4687.
[17] C. Meng, F. Lu, H. Cui, X. Tang, Research on formation and stability of keyhole in stationary laser welding on aluminum MMCs reinforced with particles, Int. J. Adv. Manuf. Technol. 67 (2013) 2917–2925, https://doi.org/10.1007/s00170-012-4704-0.
[18] Y. Kawahito, Y. Uemura, Y. Doi, M. Mizutani, K. Nishimoto, H. Kawakami, M. Tanaka, H. Fujii, K. Nakata, S. Katayama, Elucidation of the effect of welding speed on melt flows in high-brightness and high-power laser welding of stainless steel on basis of three-dimensional X-ray transmission in situ observation, Weld. Int. 31 (2017) 206–213, https://doi.org/10.1080/09507116.2016.1223204.
[19] A.A. Martin, N.P. Calta, J.A. Hammons, S.A. Khairallah, M.H. Nielsen, R. M. Shuttlesworth, N. Sinclair, M.J. Matthews, J.R. Jeffries, T.M. Willey, J.R. Lee, Ultrafast dynamics of laser-metal interactions in additive manufacturing alloys captured by in situ X-ray imaging, Mater. Today Adv. 1 (2019), 100002.
[20] Y. Chen, S.J. Clark, C.L.A. Leung, L. Sinclair, S. Marussi, M.P. Olbinado, E. Boller, A. Rack, I. Todd, P.D. Lee, In-situ Synchrotron imaging of keyhole mode multi-layer laser powder bed fusion additive manufacturing, Appl. Mater. Today 20 (2020), 100650, https://doi.org/10.1016/j.apmt.2020.100650.
[21] C. Zhao, N.D. Parab, X. Li, K. Fezzaa, W. Tan, A.D. Rollett, T. Sun, Critical instability at moving keyhole tip generates porosity in laser melting, Science 370 (2020) 1080–1086, https://doi.org/10.1126/science.abd1587.
[22] Q. Guo, C. Zhao, L.I. Escano, Z. Young, L. Xiong, K. Fezzaa, W. Everhart, B. Brown, T. Sun, L. Chen, Transient dynamics of powder spattering in laser powder bed fusion additive manufacturing process revealed by in-situ high-speed high-energy x-ray imaging, Acta Mater. 151 (2018) 169–180, https://doi.org/10.1016/j.actamat.2018.03.036.
[23] L. Wang, Y. Zhang, W. Yan, Evaporation model for keyhole dynamics during additive manufacturing of metal, Phys. Rev. Appl. 14 (6) (2020), 064039, https://doi.org/10.1103/PhysRevApplied.14.064039.
[24] E.J.R. Parteli, T. Pöschel, Particle-based simulation of powder application in additive manufacturing, Powder Technol. 288 (2016) 96–102, https://doi.org/10.1016/j.powtec.2015.10.035.
[25] H. Chen, Q. Wei, Y. Zhang, F. Chen, Y. Shi, W. Yan, Powder–spreading mechanisms in powder-bed-based additive manufacturing: experiments and computational modeling, Acta Mater. 179 (2019) 158–171, https://doi.org/10.1016/j.actamat.2019.08.030.
[26] J.H. Cho, S.J. Na, Theoretical analysis of keyhole dynamics in polarized laser drilling, J. Phys. D Appl. Phys. 40 (2007) 7638–7647, https://doi.org/10.1088/0022-3727/40/24/007.
[27] Z. Sun, Y.H. Chueh, L. Li, Multiphase mesoscopic simulation of multiple and functionally gradient materials laser powder bed fusion additive manufacturing processes, Addit. Manuf. 35 (2020), 101448, https://doi.org/10.1016/j.addma.2020.101448.
[28] D. Dai, D. Gu, Thermal behavior and densification mechanism during selective laser melting of copper matrix composites: simulation and experiments, Mater. Des. 55 (2014) 482–491, https://doi.org/10.1016/j.matdes.2013.10.006.
[29] L.Q. Chen, Phase-field models for microstructure evolution, Ann. Rev. Mater. Res. 32 (2002) 113–140, https://doi.org/10.1146/annurev.matsci.32.112001.132041.
[30] I. Steinbach, Phase-field model for microstructure evolution at the mesoscopic scale, Ann. Rev. Mater. Res. 43 (2013) 89–107, https://doi.org/10.1146/annurev-matsci-071312-121703.
[31] S. Sahoo, K. Chou, Phase-field simulation of microstructure evolution of Ti–6Al–4V in electron beam additive manufacturing process, Addit. Manuf. 9 (2016) 14–24, https://doi.org/10.1016/j.addma.2015.12.005.
[32] Y. Lian, Z. Gan, C. Yu, D. Kats, W.K. Liu, G. Wagner, A cellular automaton finite volume method for microstructure evolution during additive manufacturing, Mater. Des. 169 (2019), 107672, https://doi.org/10.1016/j.matdes.2019.107672.
[33] Z.C. Fang, Z.L. Wu, C.G. Huang, C. Wu, Review on residual stress in selective laser melting additive manufacturing of alloy parts, Opt. Laser Technol. 129 (2020), 106283, https://doi.org/10.1016/j.addma.2019.100835.
[34] A. Otto, M. Schmidt, Towards a universal numerical simulation model for laser material processing, Phys. Procedia 5 (2010) 35–46, https://doi.org/10.1016/j.phpro.2010.08.120.
[35] H. Chen, W. Yan, Spattering and denudation in laser powder bed fusion process: multiphase flow modelling, Acta Mater. 196 (2020) 154–167, https://doi.org/10.1016/j.actamat.2020.06.033.
[36] D. Liu, Y. Wang, Mesoscale multi-physics simulation of rapid solidification of Ti-6Al-4V alloy, Addit. Manuf. 25 (2019) 551–562, https://doi.org/10.1016/j.addma.2018.12.005.
[37] L.X. Lu, N. Sridhar, Y.W. Zhang, Phase field simulation of powder bed-based additive manufacturing, Acta Mater. 144 (2018) 801–809, https://doi.org/10.1016/j.actamat.2017.11.033.
[38] S.A. Khairallah, A.T. Anderson, A. Rubenchik, W.E. King, Laser powder-bed fusion additive manufacturing: physics of complex melt flow and formation mechanisms of pores, spatter, and denudation zones, Acta Mater. 108 (2016) 36–45.
[39] M. Gugliotti, M.S. Baptista, M.J. Politi, Surface tension gradients induced by temperature: the thermal Marangoni effect, J. Chem. Educ. 81 (2004) 824–826, https://doi.org/10.1021/ed081p824.
[40] P. Jafari, A. Masoudi, P. Irajizad, M. Nazari, V. Kashyap, B. Eslami, H. Ghasemi, Evaporation mass flux: a predictive model and experiments, Langmuir 34 (2018) 11676–11684, https://doi.org/10.1021/acs.langmuir.8b02289.
[41] Y.Q. Zu, S. He, Phase-field-based lattice Boltzmann model for incompressible binary fluid systems with density and viscosity contrasts, Phys. Rev. E. 87 (2013), 043301, https://doi.org/10.1103/PhysRevE.87.043301.
[42] A. Fakhari, T. Mitchell, C. Leonardi, D. Bolster, Improved locality of the phase-field lattice-Boltzmann model for immiscible fluids at high density ratios, Phys. Rev. E. 96 (2017), 053301, https://doi.org/10.1103/PhysRevE.96.053301.
[43] M. Boivineau, C. Cagran, D. Doytier, V. Eyraud, M.H. Nadal, B. Wilthan, G. Pottlacher, Thermophysical properties of solid and liquid Ti-6Al-4V (TA6V) alloy, Int. J. Thermophys. 27 (2016) 507–529, https://doi.org/10.1007/PL00021868.
[44] M. Keller, A. Chaudhary, S. Kelly, S. Medieros, Absorption Coefficient Characterization in Ti-6Al-4V Laser Additive Manufacturing. International Congress on Applications of Lasers & Electro-Optics, Laser Institute of America, 2006, p. 1204, https://doi.org/10.2351/1.5060759.
[45] M. Mohr, R. Wunderlich, R. Novakovic, E. Ricci, H.J. Fecht, Precise measurements of thermophysical properties of liquid Ti–6Al–4V (Ti64) alloy on board the international space station, Adv. Eng. Mater. 22 (2020), 2000169, https://doi.org/10.1002/adem.202000169.

[46] M. Bayat, A. Thanki, S. Mohanty, A. Witvrouw, S. Yang, J. Thorborg, N.S. Tiedje, J. H. Hattel, Keyhole-induced porosities in Laser-based Powder Bed Fusion (L-PBF) of Ti6Al4V: High-fidelity modelling and experimental validation, Addit. Manuf. 30 (2019), 100835, https://doi.org/10.1016/j.addma.2019.100835.

[47] Z. Gan, O.L. Kafka, N. Parab, C. Zhao, L. Fang, O. Heinonen, T. Sun, W.K. Liu, Universal scaling laws of keyhole stability and porosity in 3D printing of metals, Nat. Commun. 12 (2021) 1–8, doi: s41467-021-22704-0.

[48] E. Hecht, The Propagation of Light in Optics, fifth ed., Addison Wesley, New York, 2016.

[49] R. Rai, J.W. Elmer, T.A. Palmer, T. DebRoy, Heat transfer and fluid flow during keyhole mode laser welding of tantalum, Ti–6Al–4V, 304L stainless steel and vanadium, J. Phys. D Appl. Phys. 40 (2007) 5753, https://doi.org/10.1088/0022-3727/40/18/037.

[50] J. Kroos, U. Gratzke, M. Vicanek, G. Simon, Dynamic behaviour of the keyhole in laser welding, J. Phys. D Appl. Phys. 26 (1993) 481–486, https://doi.org/10.1088/0022-3727/26/3/022.

[51] Y.A. Mayi, M. Dal, P. Peyre, M. Bellet, C. Metton, C. Moriconi, R. Fabbro, Transient dynamics and stability of keyhole at threshold in laser powder bed fusion regime investigated by finite element modeling, J. Laser Appl. 33 (2021), 012024, https://doi.org/10.1103/PhysRevApplied.14.064039.

[52] G.K. Batchelor, An Introduction to Fluid Dynamics (Cambridge Mathematical Library), Cambridge University Press, Cambridge, 2017, https://doi.org/10.1017/CBO9780511800955.